International Journal Of
Industrial Electronics Control and Optimization
Print ISSN: 3517-2645
Online ISSN: 3568-2645
Homepage: https://ieco.usb.ac.ir/

A Multiport High Step-Up DC-DC Converter with a Bidirectional Port for Battery and Photovoltaic Panels Integration in Solar Power Plants

Hamed Abdi | Naghi Rostami | Ebrahim Babaei | Bulent Bilgehan

Faculty of Electrical and Computer Engineering, University of Tabriz, Tabriz, Iran.[1,2,3]
Engineering Faculty, Near East University, 99138 Nicosia, North Cyprus, Mersin 10, Turkey.[3,4]
Corresponding author's email: e-babaei@tabrizu.ac.ir

Article Info

Article type:
Research Article

Article history:
Received: 02-March-2025
Received in revised form: 27-April-2025
Accepted: 14-May-2025
Published online: 22-Dec-2025

Keywords:
Battery storage system,
Multi-port DC-DC converter,
Non-isolated power converter,
Solar power plant.

ABSTRACT

In solar power plants with energy storage systems (ESSs), a multi-port DC-DC converter equipped with a bidirectional port is more favorable than multiple single-input converters due to its simpler control, lower cost, and higher power density. This paper proposes a novel multiport DC-DC converter equipped with a bidirectional port for solar power plants. The proposed converter integrates a multi-input cascaded structure with a switched capacitor cell, a three-winding coupled inductor, and a bidirectional port connected to the ESS. Key advantages of the proposed converter include low normalized pick inverted voltage (NPIV) on semiconductor elements, continuous input current with low ripple, high voltage gain, common ground, and high efficiency. Furthermore, the converter can operate under different operating states, enabling flexible energy management strategies within the grid. The various operating states of the proposed converter are analyzed in steady state, and the validation of the mentioned advantages is supported by presenting comparative results with other DC-DC converters. Finally, the results obtained from the analysis of the proposed converter are validated through simulations performed utilizing a co-simulation link between MATLAB and PSCAD/EMTDC software.

I. Introduction

In recent years, due to the energy crisis and global warming caused by the excessive use of fossil fuels, the utilization of renewable energy sources (RES) has significantly increased as an alternative [1]. Among these sources, photovoltaic (PV) energy has gained popularity due to the easy accessibility of sunlight. The primary challenges of PV energy lie in its strong dependence on environmental conditions and the mismatch between its output voltage (20-40 V) and the voltage levels of the DC bus (400 V) and auxiliary equipment (12-60 V) [2]. Therefore, to manage power in the grid, an ESS is employed alongside the solar power plant as the energy buffer. Additionally, DC-DC converters are utilized as interface devices to accommodate and boost the voltage of solar panels, enabling their connection to the ESS and DC bus [3].

In traditional systems, each PV string and ESS are connected to the DC bus using separate unidirectional and bidirectional converters, respectively [4]. While these

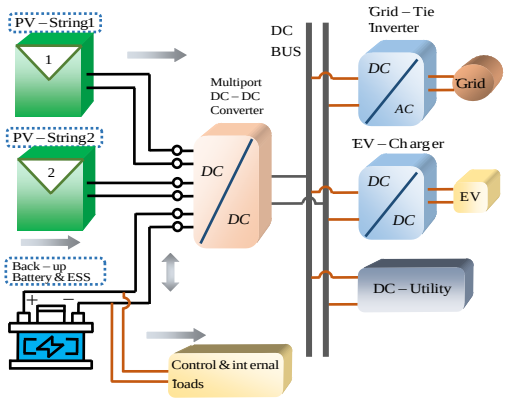


Fig. 1. Structure of DC microgrid in the presence of PV panels and ESS.

systems offer high reliability, and energy management between sources and loads becomes complex due to multiple power exchange paths. Additionally, the multiple energy conversion stages result in significant losses. So, as shown in Fig.1, employing a multi-port DC-DC converter with a

Copyright © e-babaei (s).
Publisher: University of Sistan and Baluchestan

centralized controller is a more efficient solution [5], [6].

Multi-port DC-DC converters are categorized into isolated and non-isolated types [7]. Isolated multi-port converters are not commonly utilized in RES unless galvanic isolation between the input and output and high safety is required, owing to the high cost and complexity of transformer design [8]. In contrast, non-isolated multi-port DC-DC converters are widely utilized due to their design simplicity and high voltage gain. Incorporating coupled inductors and voltage-boosting cells allows non-isolated converters to achieve high voltage gains, making them suitable for DC microgrids [9]. Voltage-boosting cells encompass various types such as switched capacitors, switched inductors, resonant capacitors, and inductor-capacitor voltage multipliers [10]. Also, in the design of non-isolated converters for PV systems, key features including input current continuity, common ground between input and output, low voltage stress on semiconductors, and high efficiency should be considered [11].

In recent years, numerous research articles on high-step-up DC-DC converters have been published in various journals. In [12] and [13], two non-isolated high step-up DC-DC converters are proposed for application in solar energy systems. These converters combine basic topologies with coupled inductors and voltage multiplier cells to enhance the voltage gain. However, despite these enhancements, the converters still suffer from low voltage gain and high power losses when operating at high-duty cycles to supply the high-voltage DC bus. In [14], a high step-up DC-DC converter with a continuous input current is proposed. Although this converter provides a high voltage gain, the absence of a defined path for the leakage current of the secondary winding of the coupled inductor leads to a high voltage spike across the output diode, thereby reducing the converter's efficiency and reliability. In [15], an interleaved DC-DC converter with high voltage gain is proposed. Owing to the integration of the interleaved structure with a coupled inductor, the converter achieves a high voltage gain while maintaining low voltage stress on the semiconductor devices. However, the absence of a common ground introduces challenges related to leakage capacitance and electromagnetic interference (EMI).

Various isolated and non-isolated multi-port DC-DC converters have been introduced in the literature in recent years. In [16], a non-isolated multi-port DC-DC converter with the ability to implement independent MPPT on its input panels is presented. However, due to the absence of a bidirectional port in this configuration, integrating an ESS with the panels is impossible, which leads to an increase in the system's size, cost, and control complexity. In [17], an isolated multi-port structure is presented. This configuration provides galvanic isolation between the input and output ports, ensuring high safety. However, due to the use of two isolation transformers and a large number of capacitors, it comes with design complexities, increased size, and higher costs. The converter presented in [18] addresses the issues mentioned in the previous sources by introducing a new path for bidirectional power flow between the battery and other ports. This converter enables the implementation of various scenarios and allows for applying different energy management algorithms (EMA) to the sources and loads. However, the extensive use of inductors and the high voltage stress on semiconductor devices have led to an increase in circuit size and volume, a reduction in converter reliability, and limitations on employing low-voltage, low-resistance switches, which in turn result in higher power losses. In [19], an isolated multi-port DC-DC converter is proposed for solar energy systems. Similar to the converter presented in [18], it offers the capability to implement various energy management scenarios. However, its practical implementation is challenged by complex commutation and the use of a three-winding isolation transformer, which complicates the design and assembly process. In [20] and [21], two non-isolated multi-port converters are proposed for applications in RES and DC motor drives, respectively. These topologies employ a combination of conventional structures with switched inductor cells to enhance voltage gain. However, the large number of elements involved makes their industrial implementation challenging.

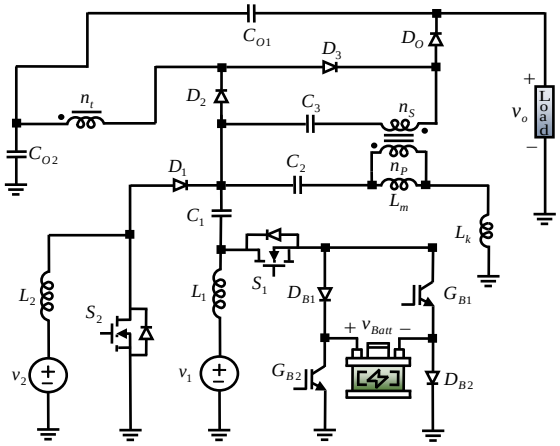


Fig. 2. Proposed structure.

Considering the challenges identified in the reviewed literature and the specific requirements for converters used in photovoltaic power plants, this paper proposes a non-isolated multi-port DC-DC converter equipped with a bidirectional port for PV applications. As depicted in Fig. 2, the proposed converter combines a cascaded multi-input topology with a switched capacitor cell, a three-winding coupled inductor, a battery, and a bidirectional port. The key features of the proposed converter include:

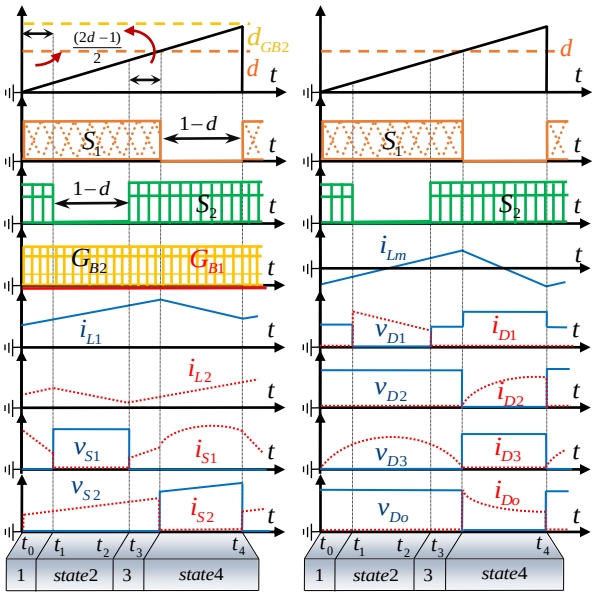
i. The ability to integrate two PV strings with a storage battery and auxiliary loads of the solar plant, which reduces volume, cost, losses, and control complexity.
ii. Common ground between the output and panel ports, which reduces the leakage capacitance.

iii. High voltage gain and continuous input current with a very low ripple in panel ports.
iv. Low voltage stress across semiconductor elements.
v. The ability to operate in different operating states, facilitating the implementation of various energy management strategies within the grid.

The remainder of the paper is organized as follows. Section II presents the elements of the proposed converter and explains its different operating states. In Section III, the steady-state analysis of the converter is carried out, along with design considerations for its elements. Section IV provides the results of the loss analysis. In Section V, the feasibility of implementing various EMAs using the converter is evaluated through a comprehensive control strategy. Sections VI, VII, and VIII, respectively, discuss the comparison study, simulation results, and conclusions.

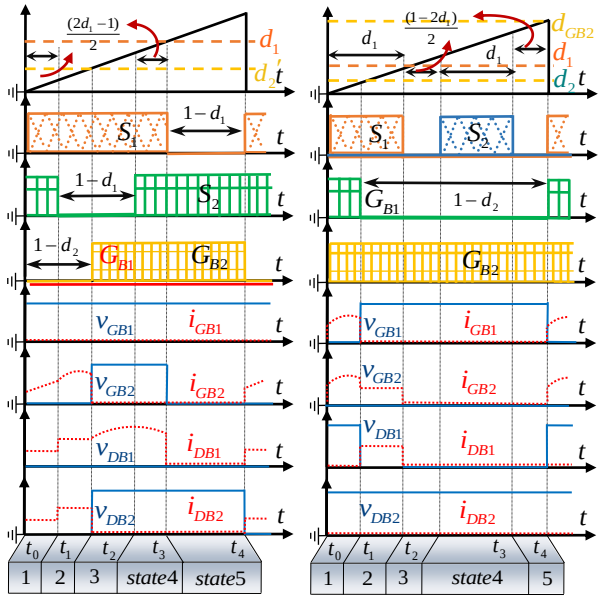
II. Proposed Structure and Operation Principles

As depicted in Fig. 2, the proposed converter comprises two MOSFETs (S_1 and S_2), two IGBTs (G_{B1} and G_{B2}), six diodes ($D_1 - D_3$, D_O, D_{B1}, and D_{B2}), five capacitors (C_1 - C_3, C_{O1} and C_{O2}), two inductors (L_1 and L_1), and a coupled inductor with turn ratios of n_1 (n_S/n_P) and n_2 (n_t/n_P). The proposed converter operates in three different operating states, with the switching waveforms of the switches as well as the current and voltage waveforms of the diodes and switches illustrated in Figs. 3 and 4. Also, the equivalent circuits corresponding to the sub-modes of the proposed converter are presented in Fig. 5. The switching waveforms are illustrated under steady-state conditions, considering component parasitics. In the equations, L_m and L_k represent magnetizing and leakage inductances, respectively, with the coupling coefficient defined as $k = L_m / (L_m + L_k)$. Also, the



(a) (b)

Fig. 3. Switching waveforms of the proposed converter in state 1.



(a) (b)

Fig. 4. Switching waveforms of the proposed converter in different states. (a) state 1 and (b) state 2.

switching pattern of the proposed converter is also presented in Table I. This table provides information regarding the on/off states of switches and diodes, the charging and discharging behavior of passive components, and the battery's operational status in different operating modes.

A. First Operating State [DISO State]

Sub-modes 1 and 3 ([$t_0 \sim t_1$] and [$t_2 \sim t_3$], [Fig.5(a)]): In mode 1, as depicted in Fig. 3, switch S_1 is turned on upon receiving a pulse and remains ON during mode 3 as well. Similarly, switch S_2 is turned on at the beginning of mode 3 and remains ON in mode 1, leading to the reverse biasing of diodes D_1, D_2, and D_O and the forward biasing of diode D_3 in both sub-modes. Also, during these sub-modes, inductors L_1 and L_2 are charged by their respective input sources, while C_{O1} and C_{O2} supply the output load. Simultaneously, C_2 charges both the magnetizing inductor L_m and capacitor C_1.

Sub-mode 2 ([$t_1 \sim t_2$], [Fig.5(b)]): In mode 2, as depicted in Fig. 3, switch S_1 is still ON while switch S_2 is turned off at the beginning of the interval, leading to the reverse biasing of diodes D_2 and D_O and the forward biasing of diodes D_1 and D_3. Also, during this sub-mode, L_1 is charged by input source V_{in1}, while L_2 charges capacitor C_1; and capacitors C_{O1} and C_{O2} supply the output load. Simultaneously, capacitor C_2 charges both the magnetizing inductor L_m and capacitor C_1.

Sub-mode 4 ([$t_3 \sim t_4$], [Fig.5(c)]): As depicted in Fig. 3, in mode 4, switch S_1 is turned off at the beginning of the interval while switch S_2 is turned on upon receiving a pulse, leading to the reverse biasing of diodes D_1 and D_3 and the forward biasing of diodes D_2 and D_O. During this sub-mode, inductor L_2 is charged by input source V_{in2}, while inductor L_2 and capacitor C_1 charge capacitor C_2 and supply the load.

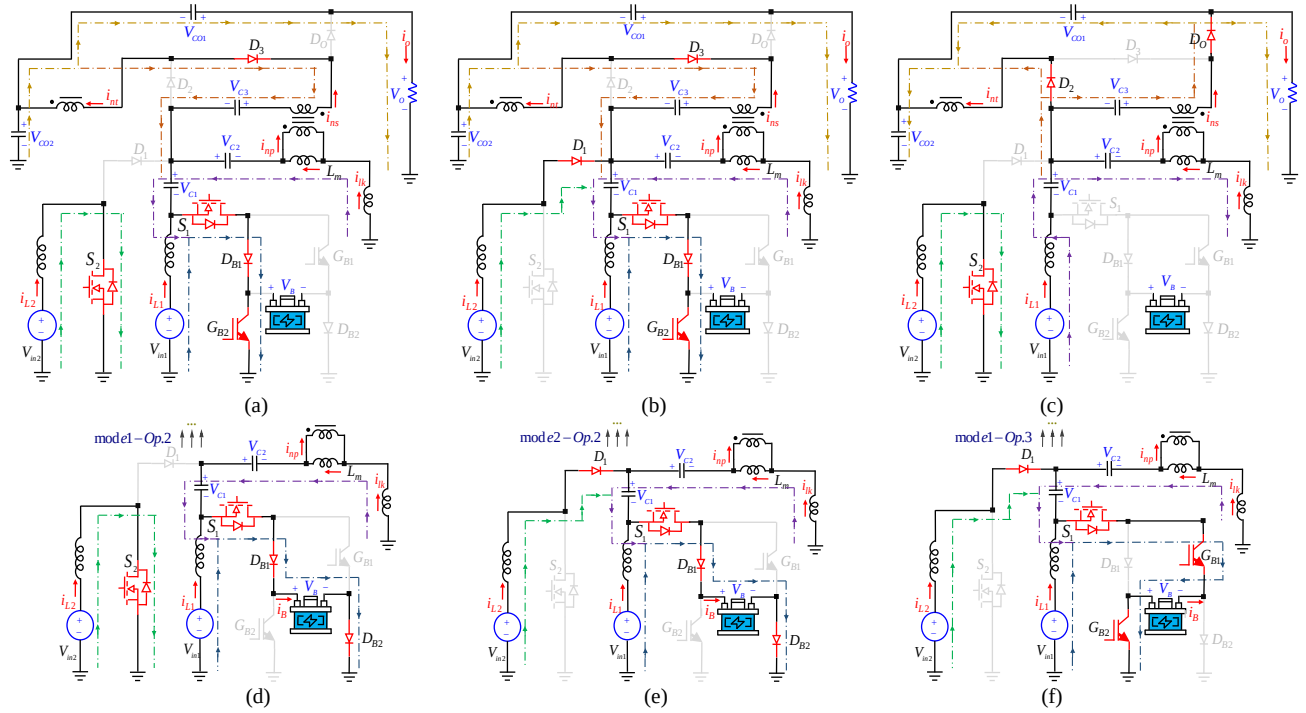


Fig. 5. Equivalent circuits related to different modes of the proposed converter in operating states 1,2, and 3. (a) State 1-mode 1 and 3, (b) State 1-mode 2, (c) State 1-mode 4, (d) State 2-mode 1, (e) State 2-mode 2, (f) State 3- mode 1.

Simultaneously, capacitor C_3 and the magnetizing inductor L_m charge capacitors C_{O1} and C_{O2} and supply the load.

B. Second Operating State [DIDO State]

This state corresponds to scenarios where the power generated by the panels exceeds the bus's demand or when the battery's state of charge (SOC) is low. As depicted in Fig. 4(a), it consists of five sub-modes. As evident from Fig. 4(a), with full turning off of switch G_{B1} and a delayed commutation of switch G_{B2}, the input sources charge the battery during sub-modes 1 and 2 (Figs. 5(d) and (e)), and the output load is supplied by the input panels simultaneously. Also, detailed patterns of switch and diode states are provided in Table I.

C. Third Operating State [TISO State]

This state pertains to scenarios where the power demanded by the DC bus exceeds the power generated by the panels and the SOC of the battery is high, prompting the battery to enter the discharge mode. As shown in Fig. 4(b), it consists of five sub-modes. As evident from Fig. 4(b), with full commutation of switch G_{B2} and commutation of switch G_{B2} in sub-mode 1, the battery is discharged to the load during sub-mode 1 (Fig. 5(f)). Also, detailed patterns of switch and diode turn-on and turn-off sequences are provided in Table I.

III. Steady-State Analysis of the Converter

A. Voltage Analysis

By applying Kirchhoff's Voltage Law (KVL) to the sub-modes corresponding to the first operating state of the proposed converter, the voltage across the magnetic elements during the ON-state of switch S_1 can be derived as follows:

$$V_{L1}{}^{ON} = V_{in1} \quad (1)$$

$$V_{L2}{}^{ON} = V_{in2} \quad (2)$$

$$V_{Lm}{}^{ON} = kV_{in1} \quad (3)$$

Similarly, by performing the same analysis during the OFF-state of switch S_1, the voltages across the magnetic elements can be calculated as follows:

$$V_{L1}{}^{OFF} = -\frac{dV_{in1}}{(1-d)} \quad (4)$$

$$V_{L2}{}^{OFF} = -\frac{dV_{in2}}{(1-d)} \quad (5)$$

$$V_{Lm}{}^{OFF} = -\frac{dkV_{in1}}{(1-d)} \quad (6)$$

Also, utilizing the volt-second balance principle for the inductors in the first operating state, the capacitor voltage relations can be expressed as follows:

$$V_{C1} = \frac{V_{in2}}{1-d} \quad (7)$$

$$V_{C2} = \frac{(1-d)V_{in1}+V_{in2}}{1-d} \quad (8)$$

$$V_{C3} = \frac{n_1k(1-d)+n_2k+1}{1-d}V_{in1} \quad (9)$$

$$V_{CO1} = \frac{k(n_1+n_2-n_2d)+1}{1-d}V_{in1} \quad (10)$$

$$V_{CO2} = \frac{(n_2kd+1)V_{in1}+V_{in2}}{1-d} \quad (11)$$

Considering (7) - (11), and utilizing KVL, the output voltage can be written as:

$$V_{O,OP1} = \frac{(k(n_1+n_2)+2)V_{in1}+V_{in2}}{(1-d)} \quad (12)$$

By applying an approach similar to that used for the first state, the capacitors and output voltage relationships for the second operating state can be derived as follows:

$$V_{C1} = \frac{2V_{in2}-(3-2d_2-2d_1)V_B}{2(1-d_1)} \quad (13)$$

TABLE I Switching Pattern of the Proposed Converter in Different States

Modes	Sub-modes	Duration	Input Port 1 (charge=Ch)	Input Port 2 (charge=Ch)	Batt. Port	Gate Signals				Diodes State (ON=1 / OFF=0)						Active Ports
						S_1	S_2	GB_1	GB_2	D_1	D_2	D_3	D_O	DB_1	DB_2	
1: No Battery Contrib-ution	1-1	$(2d-1)/2$	Ch-L_1	Ch-L_2	OFF	1	1	0	1	0	0	1	0	1	0	3
	1-2	$(1-d)$	Ch-L_1	Ch-C_1	OFF	1	0	0	1	1	0	1	0	1	0	3
	1-3	$(2d-1)/2$	Ch-L_1	Ch-L_2	OFF	1	1	0	1	0	0	1	0	1	0	3
	1-4	$(1-d)$	Supply-R_O	Ch-L_2	OFF	0	1	0	1	0	1	0	1	0	0	3
2: Battery Char-ging	2-1	$(2d_1-1)/2$	Ch-L_1/Batt	Ch-L_2	ON	1	1	0	0	0	0	0	0	1	1	4
	2-2	$\frac{3-2(d_1+d_2)}{2}$	Ch-L_1/Batt	Ch-C_1/Batt	ON	1	0	0	0	1	0	0	0	1	1	4
	2-3	$(2d_2-1)/2$	Ch-L_1	Ch-C_1	OFF	1	0	0	1	1	0	1	0	1	0	3
	2-4	$(2d_1-1)/2$	Ch-L_1	Ch-L_2	OFF	1	1	0	1	0	0	1	0	1	0	3
	2-5	$(1-d_1)$	Supply-R_O	Ch-L_2	OFF	0	1	0	1	0	1	0	1	0	0	3
3: Battery Dischar-ging	3-1	d_2	Ch-L_1	Ch-C_1	ON	1	0	1	1	1	0	1	0	0	0	4
	3-2	d_1-d_2	Ch-L_1	Ch-C_1	OFF	1	0	0	1	1	0	0	0	1	0	3
	3-3	$(1-2d_1)/2$	Supply-R_O	Supply-R_O	OFF	0	0	0	1	1	0	0	1	0	0	3
	3-4	$d_1\ d_1$	Supply-R_O	Ch-L_2	OFF	0	1	0	1	0	1	0	1	0	0	3
	3-5	$(1-2d_1)/2$	Supply-R_O	Supply-R_O	OFF	0	0	0	1	1	1	0	1	0	0	3

TABLE II Defining α and ξ coefficients

$\alpha_1 = kn_1(1-d_1) + kn_2 + 1$	$\alpha_2 = kn_2(1-d_1) + kn_1 + 1$	$\alpha_3 = 2(1 + kn_2d_1)$
$\alpha_4 = 4 + 2kn_2 + 2kn_1$	$\alpha_5 = {d_1}^2(1+kn_1) - d_1(kn_2 + 2n_1k - 1) + k(n_1+n_1)$	$\alpha_6 = {d_1}^2(1+kn_2) - d_1(kn_1 + 2n_2k - 1) + k(n_1+n_1)$
$\alpha_7 = d_1(1 + kn_2 - d_1kn_2)$	$\alpha_8 = {d_1}^2 + d_1(2 - kn_2 - n_1k) + k(n_1+n_1)$	
$\zeta_1 = {d_1}^2 + d_1(2 - kn_2 - n_1k) + k(n_1+n_1)$	$\zeta_2 = kn_1(d_1-1) - 1 + d_2 + (k - 1 - kd_1 + d_1)$	$\zeta_3 = -(5 - 4d_2 - 2d_1 + 2n_2k(1-d_2))$
$\xi_5 = {d_1}^2(kn_1 + kn_2 + 1) - d_1(2kn_1 + 2kn_2 + d_2kn_2 + d_2 + 2) + (kn_1 + kn_2 + 1 + d_2(1+n_2k))$	$\xi_6 = {d_1}^2(kn_1 + kn_2 + 1) - d_1(2kn_1 + 2kn_2 + d_2kn_1 + d_2 + 2) + (kn_1 + kn_2 + 1 + d_2(1+n_1k))$	$\xi_8 = {d_1}^2(kn_1 + kn_2 + 1) - d_1(2kn_1 + 2kn_2 + d_2kn_1 + d_2kn_2 + d_2 + 2) + (kn_1 + kn_2 + 1 + d_2(2 + n_1k + n_2k))$
$\zeta_4 = 8d_2 - 9 - 2kn_1(1-d_1) + 2k + 2d_1 - 2k(n_2 + d_2 - d_2n_2)$	$\zeta_7 = d_2(1 + n_2k - d_1n_2k)$	

$$V_{C2} = \frac{2(1-d_1)V_{in1} + 2V_{in2} - (3-2d_2-2d_1)V_B}{2(1-d_1)} \quad (14)$$

$$V_{C3} = \frac{\alpha_1 V_{in1} + \xi_1 V_B}{(1-d_1)} \quad (15)$$

$$V_{CO1} = \frac{\alpha_2 V_{in1} + \xi_2 V_B}{(1-d_1)} \quad (16)$$

$$V_{CO2} = \frac{\alpha_3 V_{in1} + 2V_{in2} + \xi_3 V_B}{2(1-d_1)} \quad (17)$$

$$V_{O,OP2} = \frac{\alpha_4 V_{in1} + 2V_{in2} + \xi_4 V_B}{2(1-d_1)} \quad (18)$$

Furthermore, it can be written for the third state as follows:

$$V_{C1} = \frac{(2d_1-1)V_{in1} + (1-d_1)V_{in2} + d_1d_2V_B}{(1-d_1)^2} \quad (19)$$

$$V_{C2} = \frac{\alpha_1 V_{in1} + \xi_1 V_B}{(1-d_1)} \quad (20)$$

$$V_{C3} = \frac{\alpha_5 V_{in1} + \xi_5 V_B}{(1-d_1)^2} \quad (21)$$

$$V_{CO1} = \frac{\alpha_6 V_{in1} + \xi_6 V_B}{(1-d_1)^2} \quad (22)$$

$$V_{CO2} = \frac{\alpha_7 V_{in1} + (1-d_1)V_{in2} + \xi_7 V_B}{(1-d_1)^2} \quad (23)$$

$$V_{O,OP3} = \frac{\alpha_8 V_{in1} + (1-d_1)V_{in2} + \xi_8 V_B}{(1-d_1)^2} \quad (24)$$

Also, α_1-α_8 and ξ_1-ξ_8 coefficients are defined in Table II.

B. Current Analysis

By neglecting the power losses of the converter and using Kirchhoff's Current Law (KCL) along with the average model, the average current of the magnetizing elements in the converter during the first operating state is calculated as follows:

$$I_{L1} = \frac{n_1+n_2+2}{(1-d)} I_O \quad (25)$$

$$I_{L2} = \frac{1}{(1-d)} I_O \quad (26)$$

$$I_{Lm} = 0 \quad (27)$$

Also, the coupled inductor winding currents are calculated as presented in Table III. Furthermore, the battery's instantaneous currents in sub-modes corresponding to states 2 and 3 are also listed in Table III. For calculating the average battery current, only the instantaneous currents in sub-modes 1 and 2 of the second state and sub-mode 1 of the third state are used. Moreover, the instantaneous currents of the capacitors in the first state and their corresponding RMS values are calculated and presented in Table IV.

C. Voltage and Current Stress of Semiconductors

Among the critical factors in selecting switches and diodes for converters are their voltage and current stresses. The NPIV of a switch represents the voltage across it during its off-state. Similarly, the current stress refers to the instantaneous current flowing through the switch during its operation. Based on these considerations, NPIV, current stresses, and rms current of switches and diodes of the converter are calculated and presented in Table V.

D. Boundary Conduction Mode

For the proposed converter to operate in continuous conduction mode (CCM), the minimum current of the input inductors must remain greater than zero. Considering this condition, along with (26) and by applying KVL in the

TABLE III Battery and coupled-inductor current relations

States	i_B in different sub-modes (Instantaneous current)
State. 2	$i_B{}^1 = \frac{n_1+n_2+2}{(1-d_1)} I_O \quad i_B{}^2 = \frac{n_1+n_2+3}{(1-d_1)} I_O \quad i_B{}^5 = 0$ $i_B{}^3 = \frac{(1-d_1)(n_1+n_2)+(d_1+d_2-1)(n_1+n_2+3)}{(1-d_1)(d_1+d_2-1)} I_O$ $i_B{}^4 = \frac{(1-d_1)(n_1+n_2)+(d_1+d_2-1)(n_1+n_2+2)}{(1-d_1)(d_1+d_2-1)} I_O$
State. 3	$i_B{}^1 = i_B{}^2 = \frac{n_1+n_2+2d_1+1}{d_1(1-d_1)} I_O$
States	I_B in different modes (Average current)
State. 2	$I_B = \frac{2(n_1+n_2)+7-2d_1-2d_2(n_1+n_2+3)}{2(1-d_1)} I_O$
State. 3	$I_B = \frac{d_2(n_1+n_2+2d_1+1)}{d_1(1-d_1)} I_O$

Coupled-Inductor	Coupled-inductor instantaneous current in state 1		
Sub-modes	i_{np}	i_{ns}	i_{nt}
1,2,3	$-\frac{I_O}{d}(n_1+n_2)$	$-\frac{I_O}{d}$	$-\frac{I_O}{d}$
4	$\frac{I_O}{(1-d)}(n_1+n_2)$	$\frac{I_O}{(1-d)}$	$\frac{I_O}{(1-d)}$

TABLE IV Capacitors' currents in state 1

Element	Mode 1	Mode 2	
C_1	$\frac{n_1+n_2+1}{4d} I_O$	$\frac{n_1(1-d)+n_2(1-d)+1}{d(1-d)} I_O$	
Element	Mode 3	Mode 4	RMS
C_1	$\frac{3(n_1+n_2+1)}{4d} I_O$	$-\frac{n_1+n_2+2}{(1-d)} I_O$	$\frac{n_1+n_2+2}{\sqrt{d(1-d)}} I_O$
Element	Modes 1, 2, 3	Mode 4	RMS
C_2	$-\frac{(n_1+n_2)}{d} I_O$	$\frac{(n_1+n_2)}{(1-d)} I_O$	$\frac{n_1+n_2}{\sqrt{d(1-d)}} I_O$
C_3	$\frac{1}{d} I_O$	$-\frac{1}{(1-d)} I_O$	$\frac{1}{\sqrt{d(1-d)}} I_O$
C_{O1}	$-I_O$	$\frac{d}{(1-d)} I_O$	$\frac{\sqrt{d}}{\sqrt{(1-d)}} I_O$
C_{O2}	$-\frac{1+d}{d} I_O$	$\frac{1+d}{(1-d)} I_O$	$\frac{1+d}{\sqrt{d(1-d)}} I_O$
L_k	$\frac{(n_1+n_2)}{d} I_O$	$-\frac{(n_1+n_2)}{(1-d)} I_O$	$\frac{n_1+n_2}{\sqrt{d(1-d)}} I_O$

corresponding sub-modes, the following condition for CCM operation with inductor L_2 can be derived.

$$L_2 > \frac{d(1-d)^2 R_O}{2(n_1+n_2+3) f_S} \quad (28)$$

Additionally, the graph related to this condition is plotted in Fig. 6, illustrating the values of inductor L_2 for continuous, discontinuous, and boundary conduction modes.

IV. Efficiency Analysis Results

In this section of the paper, the losses of the proposed converter are calculated following the procedure outlined in [22]. To avoid unnecessary length, only the final results are presented. In these calculations, the losses considered include conduction and switching losses of the switches and diodes, conduction losses of the capacitors, as well as both core and conduction losses of the inductors and the coupled inductor. So, based on the calculated losses, the overall efficiency of the converter is obtained using the following:

TABLE V Voltage and current stress of semiconductors

S,D		Instantaneous	RMS	NPIV
S_1	Mode 1	$\frac{(1+3d)(n_1+n_2+1)+4}{4d(1-d)}$		
	Mode 2	$\frac{n_1+n_2+1+2d}{d(1-d)} I_O$	$\frac{(n_1+n_2+2)I_O}{(1-d)\sqrt{d}}$	$\frac{V_O}{2n+3}$
	Mode 3	$\frac{(7-3d)(n_1+n_2+1)+4}{4d(1-d)}$		
S_2		$\frac{I_O}{(1-d)}$	$\frac{\sqrt{d} I_O}{(1-d)}$	$\frac{V_O}{2n+3}$
D_1		$\frac{I_O}{(1-d)}$	$\frac{I_O}{\sqrt{(1-d)}}$	$\frac{2V_O}{2n+3}$
D_2		$\frac{I_O}{(1-d)}$	$\frac{I_O}{\sqrt{(1-d)}}$	$\frac{(1+n)V_O}{2n+3}$
D_3		$\frac{I_O}{d}$	$\frac{I_O}{\sqrt{d}}$	$\frac{(1+2n)V}{2n+3}$
D_O		$\frac{I_O}{(1-d)}$	$\frac{I_O}{\sqrt{(1-d)}}$	$\frac{(1+n)V_O}{2n+3}$

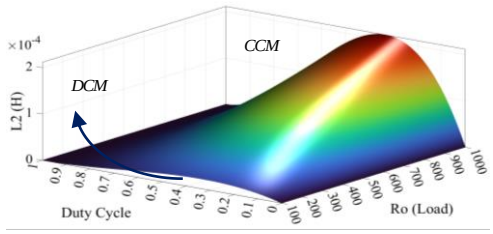


Fig. 6. Boundary condition for inductor L_2.

$$\eta(\%) = \frac{(P_{out})\times 100}{(P_{out}+(P_{cond,L}+P_{core,L}+P_{cond,S,D}+P_{sw,S,D}+P_{cond,C}))} \quad (29)$$

The calculated results for the efficiency and power losses of the proposed converter in the first operating state are illustrated in Figs. 7 and 8. Fig. 7(a) presents the efficiency of the proposed converter at various power levels and input voltages. As shown in this figure, the maximum efficiency of the converter is achieved at an output power of 100 W for all considered input voltages. Figs. 7(b) and (c) illustrate the percentage of power losses associated with different elements of the converter under various input voltages.

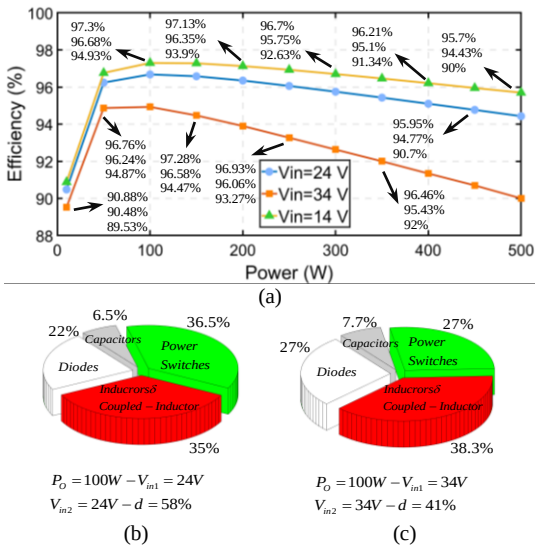


Fig. 7. (a) Efficiency curves of the proposed converter in different powers, (b) and (c) Loss percentage of the converter in different input voltages.

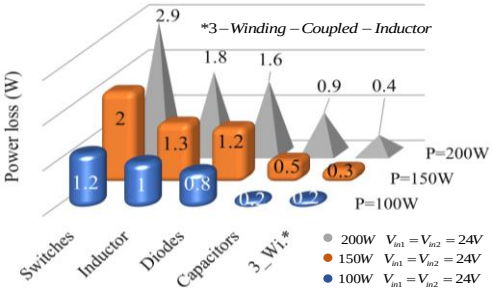


Fig. 8. Loss distribution of the converter in different powers.

V. Energy Management Algorithm for the Proposed Converter

To assess the converter's performance under various energy management conditions, it is tested using an algorithm similar to [5], shown in Fig. 9. The algorithm considers the internal loads, battery, PV panels, and DC/AC buses as system inputs/outputs, assuming normal grid and load operation. In the evening, the battery's charge rate is increased to support night-time loads. Energy management mainly depends on grid demand, PV generation, and battery SOC. If PV power is insufficient, the battery supplies the load (Scenario 3); otherwise, excess energy charges the battery or feeds auxiliary loads.

VI. Comparison Study

This section compares the proposed converter with other recent dual- and multi-port high-step-up DC-DC converters. Key specs from [6], [18], [23]–[27] are listed in Table VI, and cost estimates appear in Table VII, based on components selected for the simulation power level. Comparative analysis includes voltage gain (Figs. 10(a) and b), voltage stress (Fig. 10(c)), cost (Figs. 11(a)), and efficiency (Fig. 11(b)), using standard components detailed in Table VIII. The evaluation covers voltage gain, stress, ripple, EMI, element count, efficiency, cost, number of ports, and supported operating scenarios.

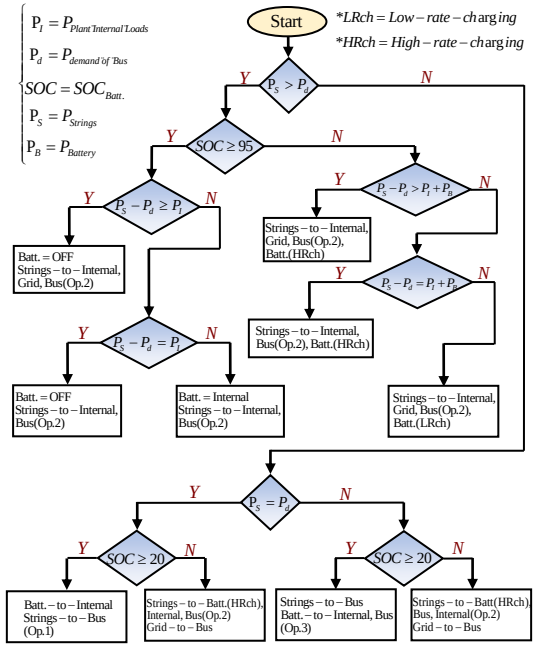


Fig. 9. Energy management algorithm for the proposed converter

As shown in Table VI and Fig. 10(a), the proposed converter achieves the highest voltage gain—27 at a 0.5 duty cycle—about 15 units more than converters [18], [25], and [26]. This is due to its use of a three-winding coupled inductor and a switched-capacitor cell, unlike [25] with only two windings and [18], [26] which lack coupled inductors.

As shown in Table IV, aside from converter [24], the proposed converter and converter [17] have the highest number of elements. This is due to their multiple ports and support for various operating scenarios, which require additional auxiliary components. Both topologies allow independent battery switching within multi-input structures, enabling flexible energy management through simpler control and relatively fewer total components. According to Fig. 10(b), the proposed converter achieves a voltage gain-to-

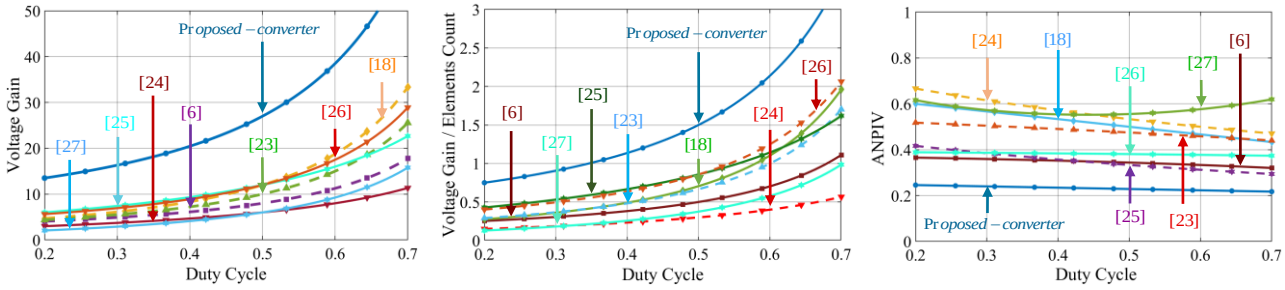
TABLE VI Detailed specifications of the proposed converter and the converters proposed in [6], [18], [23], [24], [25], [26], and [27]

Parameters		Multi-port Converters					Dual-Port Converters		Proposed Converter
		[6]	[18]	[23]	[24]	[25]	[26]	[27]	
Elements*	S	4	4	6	4	2	1	1	4
	D	4	5	1	6	4	6	5	6
	C	4	4	4	8	5	5	7	5
	L	4	4	4	0	2	2	4	2
	T/CI	0	0	0	2	1	0	0	1
	Total	16	17	15	20	14	14	16	18
Voltage gain		$\frac{3-2d}{(1-d)^2}$	$\frac{3}{(1-d)^2}$	$\frac{3-d}{(1-d)^2}$	$\frac{n(1+d)}{(1-d)}$	$\frac{4+2nd}{(1-d)}$	$\frac{2(2-d)}{(1-d)^2}$	$\frac{1+2d-2d^2}{(1-d)^2}$	$\frac{4n+2+d+d^2-4dn}{(1-d)^2}$
Inputs/outputs		3/1	2/1 – 3/1 – 2/2	2/1	1/2	2/1	1/1	1/1	2/1 – 3/1 – 2/2
Non-isolated		Yes	Yes	Yes	No	Yes	Yes	Yes	Yes
EMI		Low	Low	Low	Low	High	High	Low	Low
ANPIV		$\frac{9-7d}{8(3-2d)}$	$\frac{18-9d}{27}$	$\frac{13-7d}{8(3-d)}$	$\frac{4+6n}{10n(1+d)}$	$\frac{4+n}{6(2+nd)}$	$\frac{11-6d}{14(2-d)}$	$\frac{5+2d^2-d}{6(1+2d-2d^2)}$	$\frac{11+4n-4d}{20n+30}V_o$
I.C.R.*		Low	Low	Low	High	Low	Low	Low	Low
η (%)		Not given	94.2% (100 W)	94% (100 W)	95.5% (250 W)	93.34% (100 W))	94.6% (100 W)	85.4% (100 W)	96.68% (100 W)

*S**: Switch, *D**: Diode, *C**: Capacitor, *I**: Inductor, *T**: Transformer, *CI**: Coupled inductor, *I.C.R.**: Input current ripple.

TABLE VII Cost calculations of the proposed converter and the converters in [6], [18], and [24]-[26].

Ref.	Switches Cost	Diodes Cost	Capacitors Cost	Cores Cost	Total Cost
[6]	4*0.42 $	4*1.06 $	1*0.1 $, 1*0.1 $ 1*0.1 $, 1*1.5 $	4*2.5 $	17.72 $
[18]	1*12.44 $, 3*1.9 $	2*0.8 $, 1*0.7 $, 2*0.31	3*0.5 $, 1*1.5 $	4*0.4 $	25.66 $
[24]	4*0.74 $	6*0.8 $	4*0.5 $, 2*6 $	3*2.5 $	26.76 $
[25]	2*0.89 $	4*0.31 $	1*0.2 $, 1*0.2 $, 1*0.53 $ 1*1 $, 1*6 $	3*2.5 $	18.45 $
[26]	1*2.15 $	5*0.57 $	1*0.2 $, 1*0.1 $, 1*0.4 $ 1*0.4 $, 1*1 $	2*2.5 $	12.1 $
Proposed	4*0.42 $	6*1.06 $	1*0.1 $, 1*0.1 $, 1*0.4 $ 1*0.4 $, 1*0.4 $	3*2.5 $	16.94 $



(a) (b) (c)

Fig. 10. Comparison graphs in n=2. (a) Voltage gain, (b) voltage gain/element count, and (c) ANPIV index.

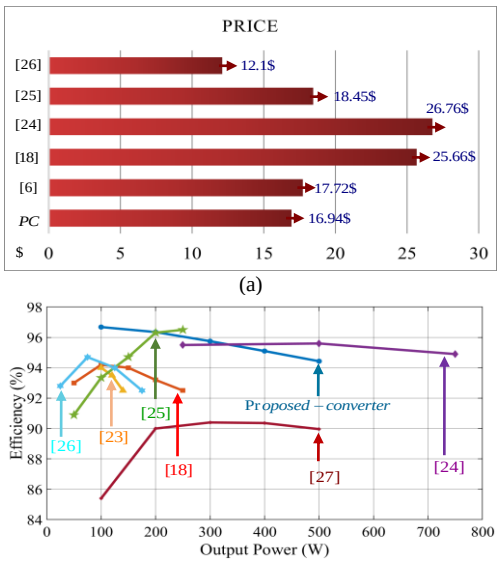
element-count ratio of 3 at a 0.5 duty cycle—0.65 higher than [25] and [26], and significantly better than [24], which has a ratio of 0.3 due to its complexity and low gain. Despite the element count, the proposed converter also reaches the highest efficiency at 100 W output power, where most compared designs peak. As shown in Fig. 11(b), it maintains high efficiency across a wide power range, thanks to selective element activation and low voltage stress on semiconductors. As shown in Table IV and Fig. 10(c), the proposed converter has the lowest ANPIV index, with switch NPIV values also below average. This is due to placing voltage-boosting cells at the final stage. In contrast, converters [18], [24], and [27] show the highest ANPIV values, as their front-end switched inductor-capacitor cells increase conduction losses and reduce reliability.

As shown in Table VI, converters [25] and [26] suffer from high EMI due to the absence of a common ground between input sources and the output. In [25], this stems from the dual-input design, and in [26], from the voltage-doubler cell. In contrast, the proposed converter features a common ground between main inputs and output, reducing high-frequency circulating currents. While the battery connection via an auxiliary diode introduces slight EMI, this is mitigated by using a low-voltage battery or EMI filters in practical setups. Although converter [24] benefits from input-output isolation and low EMI, its high input current ripple makes it less ideal for PV systems.

As indicated in Table VII, converters [6], [26], and the proposed design offer the lowest overall cost, making them suitable for large-scale deployment. In contrast, Fig. 11(a) shows that converters [18] and [24] are the most expensive due to their use of high-voltage switches and multiple magnetic elements. Overall, the proposed converter stands out as a strong candidate for solar-powered DC microgrids, thanks to its high voltage gain, low ANPIV, high efficiency, low EMI, minimal input current ripple, cost-effectiveness, and broad energy management capability.

VII. Simulation Results

This section presents the simulation results of the proposed converter in all three operating states. The



(a)

(b)

Fig. 11. (a) Cost comparison of the compared converters and (b) Efficiency comparison of the compared converters.

simulations are carried out using PSCAD software, and the data obtained are subsequently plotted using MATLAB. Also, the simulations are conducted based on the parameters listed in Table VIII, and the corresponding results are presented in Figs. 12 - 15.

Fig.12 illustrates the input and output voltages as well as the load current of the proposed converter in all three operating states. In each state, when input ports 1 and 2 are supplied with 24 V and the battery port is provided with 12 V, the converter delivers an output voltage of 400 V and an output current of 0.25 A. Figs. 13(a) – (e) depict the simulation results of the capacitor voltages in the proposed converter in the first operating state. As observed, the voltages across capacitors $C_1 - C_3$, C_{O1}, and C_{O2} are 57 , 81 , 224 , 220 , and 180 V, respectively, which confirm the values obtained from (7) - (11). Figs. 13(f) – (h) also illustrate the simulation results of the magnetic element currents in the proposed converter in the first operating state. The obtained current values for inductors L_1, L_2, and L_m are 3.7 , 0.62 , and 0 A, respectively, which validate the theoretical results derived from (25) - (27). In addition, Figs. 13(i) - (l) show the waveforms of the transformer winding currents and the leakage current. The obtained values are in good agreement with the theoretical results presented in Table III. Fig. 14 illustrates the simulated voltage and current waveforms of the semiconductors in the proposed converter during state 1. According to this figure, the voltage stresses of switches and diodes S_1, S_2, D_1, D_2, D_3, and D_O are obtained as 57, 57, 114, 170, 285, and 170 V, respectively. These results are consistent with the theoretical values calculated from the relations presented in Table V. Also, the values 6.1, 0.61, 0.6, 0.6, 0.42, and 0.62 A are obtained for I_{S1}, I_{S2}, I_{D1}, I_{D2}, I_{D3}, and I_{DO}, respectively. The obtained values follow the theoretical results presented in Table V.

Moreover, to manage the length of the paper, the complete set of simulated waveforms for operating states 2 and 3 has not been included. Instead, only the battery

TABLE VIII Simulation parameters of the proposed converter

Symbols	Values and types
Output Power	100 W
Input Voltages (V_1 and V_2)	24 V
Output voltage (V_O)	400 V
Battery voltage (V_B)	12 V
Capacitors (C_1, C_2, C_3)	47 uF/100 V, 47 uF/100 V, 47 uF/400 V
Output capacitors (C_{O1}, C_{O2})	47 uF/400 V
Input inductors (L_1, L_2)	500 uH
Magnetizing inductance (L_m)	500 uH
Leakage inductance (L_k)	1 uH
Turn ratios (n_1 and n_2)	2
Switching frequency (f_S)	50 KHz
d (State 1)	59.5%
d_1 (State 2)	66%
d_2 (State 2)	63%
d_1 (State 3)	45%
d_2 (State 3)	35%

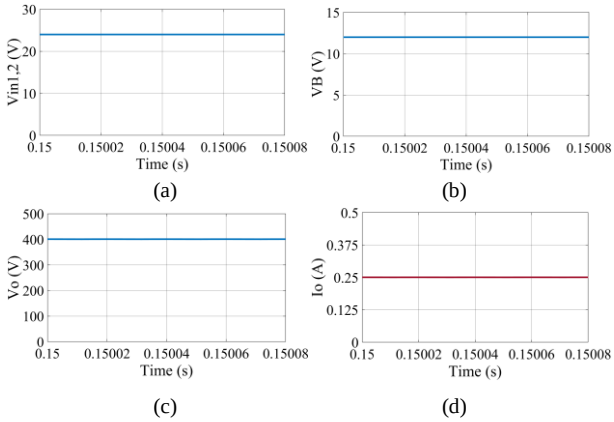


Fig. 12. Simulation results of the converter in all states

charging and discharging current waveforms for these states are presented in Fig 15. As shown in this figure, the obtained values of the battery currents are in good agreement with the calculated values presented in Table III.

Due to the dependence of the output voltage of photovoltaic (PV) panels on environmental conditions, a controller is required to stabilize the output voltage of the converter at a constant level. In the proposed converter, two control loops are needed. The first control loop is associated with the auxiliary switches, which regulate the charging and discharging power of the battery based on the algorithm presented in Fig. 9. Also, an external voltage control loop is used to regulate the output voltage of the converter. Fig. 16 illustrates a simple PI controller schematic that is applied to all operating states of the proposed converter and controls main switches S_1 and S_2. This controller receives the error between the reference and actual output voltage and generates the required pulse width to drive the switches, aiming to eliminate the voltage error.

By designing the closed-loop control system as shown in Fig. 16 and simulating it for second and third states of the proposed converter, the output voltage results under input voltage and load disturbances are obtained. These results are illustrated in Fig. 17. Fig. 17(a) illustrates the output voltage and power of the proposed converter in the second operating state. As shown, both the battery voltage and the main input source voltages remain constant, while the output load is first decreased from 1600 Ω to 533 Ω and then increased to 800 Ω. Throughout these variations, the controller demonstrates a fast dynamic response, effectively tracking the reference voltage and maintaining the output voltage at a constant 400 V. Fig. 17(b) presents the output voltage and output power of the proposed converter in the third operating state. As shown, both the output load and the battery voltage are kept constant during this state. When the main input source voltage changes from 24 V to 20 V and then returns to 28 V, the controller effectively regulates the output voltage, maintaining it at 400 V with a very short settling time.

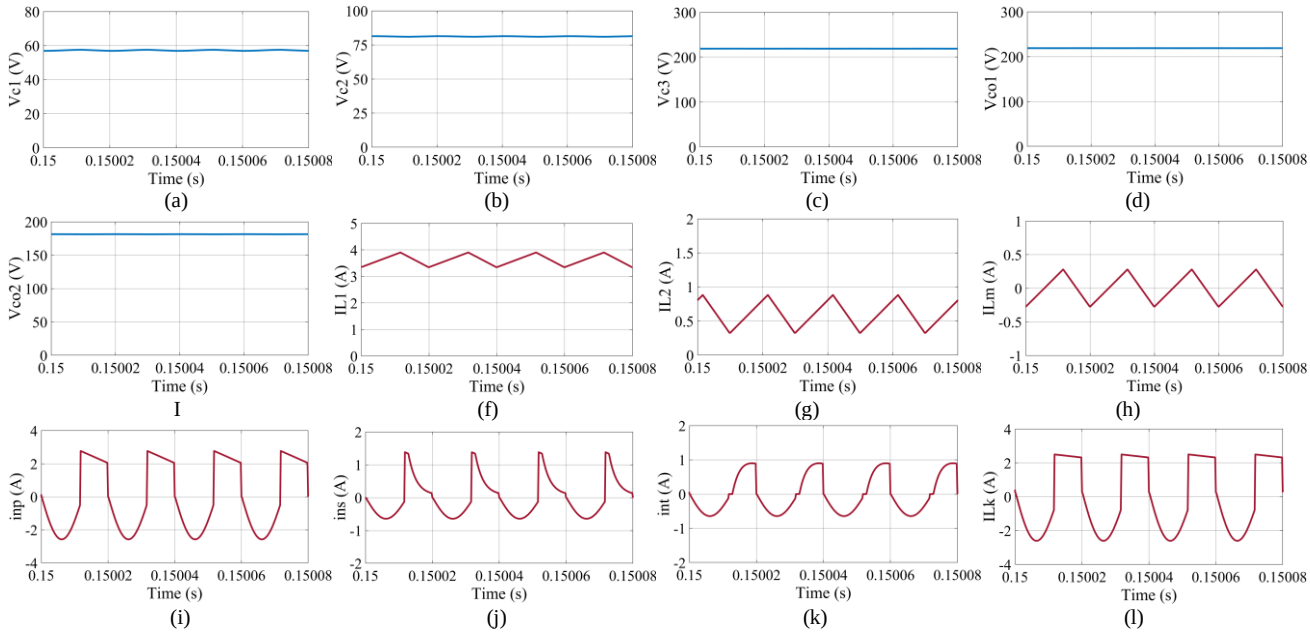


Fig. 13. Simulation results of the proposed converter in operating state 1.

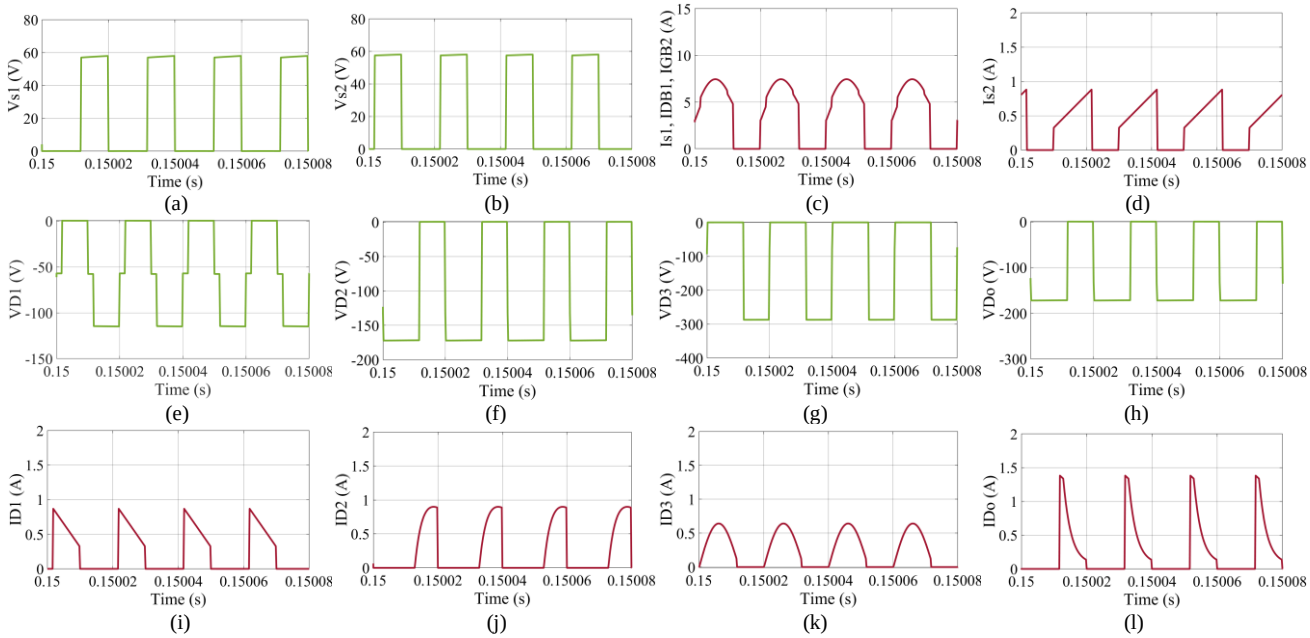


Fig. 14. Simulation results of the proposed converter in operating state 1.

VIII. Conclusion

This paper presents a non-isolated multi-port DC-DC converter equipped with a bidirectional port for integrating solar panels with storage systems in hybrid solar power plants. Based on the analysis of the proposed converter, features such as high voltage gain, low voltage stress on diodes and switches, continuous input current, high efficiency, and common ground are identified. The use of one bidirectional port and two unidirectional ports in the designed structure enables the integration of energy generation and

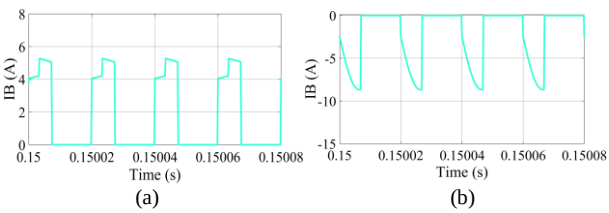


Fig. 15. Simulation results of the proposed converter for battery current. a) state 2, b) state 3.

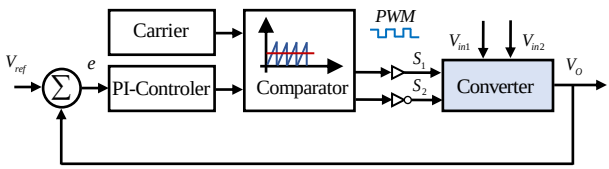
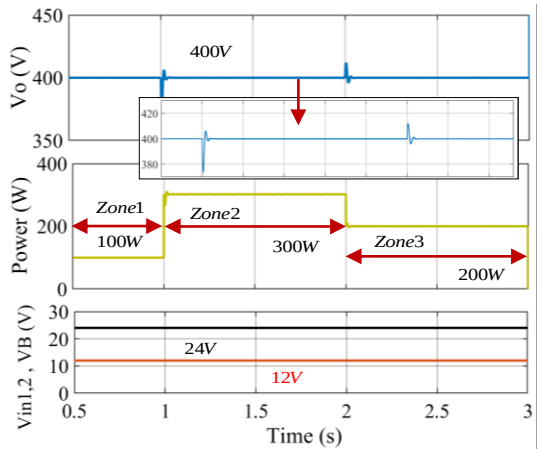
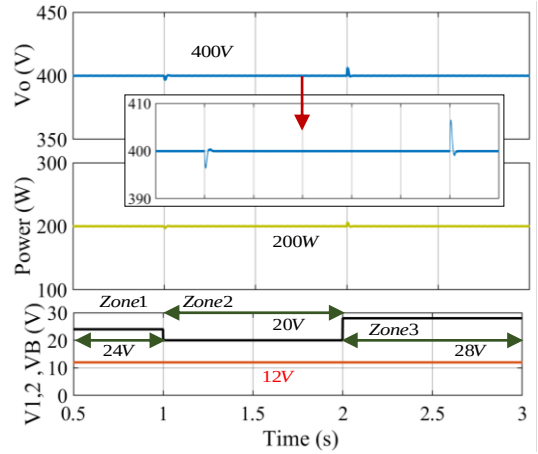


Fig. 16. Block diagram of PI controller for the proposed converter.



(a)



(b)

Fig. 17. Simulation results of the output voltage waveforms of the proposed converter under input voltage and load disturbance, (a) state 2, (b) state 3.

storage sources and reduces system complexity, volume, and losses. Additionally, its ability to operate in various operating states allows the implementation of different energy management strategies in the grid. In this regard, the feasibility of the proposed converter's operation under various energy management scenarios was examined through the development of an EMA. Furthermore, the proposed converter was analyzed in all operating states, and a comparison was conducted between it and similar structures presented in the references to validate the stated features. Finally, simulation results were utilized to validate the analysis results of the converter.

REFERENCES

[1] F. Karimian, A. Nahavandi, and P. Pakbaz, "A Novel Structure of High Voltage Gain DC-DC Converters for Photovoltaic (PV) Applications," *Engineering Reports*, vol. 7, no. 1, p. e13105, 2025.

[2] L. Li, X. Hou, and Y. Liao, "A Decentralized Optimal Economic Dispatch Control of Cascaded-Type DC Microgrids With Capacity and Load Voltage Constraints," *International Journal of Circuit Theory and Applications*, 2025.

[3] T. Falope, L. Lao, D. Hanak, and D. Huo, "Hybrid energy system integration and management for solar energy: A review," *Energy Conversion and Management: X*, p. 100527, 2024.

[4] P. Abolhassani, M. Maalandish, A. Nadermohammadi, M. B. B. Sharifian, M. R. Feyzi, and S. H. Hosseini, "A high step-up high step-down coupled inductor based bidirectional DC-DC converter with low voltage stress on switches," *IET Power Electronics*, vol. 17, no. 7, pp. 802-823, 2024.

[5] M. Dezhbord, P. Mohseni, S. H. Hosseini, D. Mirabbasi, and M. R. Islam, "A high step-up three-port DC-DC converter with reduced voltage stress for hybrid energy systems," *IEEE Journal of Emerging and Selected Topics in Industrial Electronics*, vol. 3, no. 4, pp. 998-1009, 2022.

[6] K. Varesi, A. A. Ghandomi, S. Hosseini, M. Sabahi, and E. Babaei, "An improved structure for multi-input high step-up DC-DC converters," in *2017 8th Power Electronics, Drive Systems & Technologies Conference (PEDSTC)*, 2017: IEEE, pp. 241-246.

[7] A. Nadermohammadi, M. Maalandish, A. Seifi, P. Abolhassani, S. H. Hosseini, and M. Farsadi, "A non-isolated single-switch ultra-high step-up DC-DC converter with coupled inductor and low-voltage stress on switch," *IET Power Electronics*, vol. 17, no. 2, pp. 251-265, 2024.

[8] E. E. Henao-Bravo, C. A. Ramos-Paja, A. J. Saavedra-Montes, D. González -Montoya, and J. Sierra -Pérez, "Design method of dual active bridge converters for photovoltaic systems with high voltage gain," Energies, vol. 13, no. 7, p. 1711, 2020.

[9] A. Imanlou, E. Babaei, and S. H. Hosseini, "A New High Voltage Gain Common-Ground Step-Up DC-DC Converter Integrating Coupled-Inductors and Switched-Capacitors," *International Journal of Circuit Theory and Applications*, 2024.

[10] P. Aghakhanlou *et al.*, "New Structure of Step-Up DC-DC Converter Based on Three Winding Coupled Inductor with High Gain Capability Featuring Integrated Renewable Energy Applications," 2024.

[11] A. Nadermohammadi *et al.*, "Cost-effective soft-switching ultra-high step-up DC-DC converter with high power density for DC microgrid application," *Scientific Reports*, vol. 14, no. 1, p. 20407, 2024.

[12] M. Elmi, M. R. Banaei, and H. Afsharirad, "Study on a Non-Isolated High Step-Up SEPIC-Based DC-DC Converter with Continuous Input Current for Photovoltaic Applications," *International Journal of Industrial Electronics Control and Optimization*, vol. 8, no. 1, pp. 95-104, 2025.

[13] S. Toofan, B. Fathipour, and E. Babaei, "A Single Switch Transformer-Less DC-DC Converter with Continuous Input Current for Photovoltaic Applications," *International Journal of Industrial Electronics Control and Optimization*, vol. 7, no. 4, pp. 281-290, 2024.

[14] K. Yari and S. Hasanpour, "A Minimum Phase DC-DC Converter with High Voltage Gain and Continuous Input Current," *International Journal of Industrial Electronics Control & Optimization*, vol. 7, no. 4, 2024.

[15] B. Akhlaghi, N. Molavi, M. Fekri, and H. Farzanehfard, "High step-up interleaved ZVT converter with low voltage stress and automatic current sharing," *IEEE Transactions on Industrial Electronics*, vol. 65, no. 1, pp. 291-299, 2017.

[16] E. Amiri, R. R. Khorasani, E. Adib, and A. Khoshkbar-Sadigh, "Multi-input high step-up DC-DC converter with independent control of voltage and power for hybrid renewable energy systems," *IEEE Transactions on Industrial Electronics*, vol. 68, no. 12, pp. 12079-12087, 2020.

[17] C.-L. Shen and L.-Z. Chen, "Dual-input isolated converter with dual-charge-pump cell for high step-up voltage ratio achievement," *IEEE Transactions on Industrial Electronics*, vol. 67, no. 11, pp. 9383-9392, 2019.

[18] S. Rostami, V. Abbasi, and N. Talebi, "Ultrahigh step-up

multiport DC-DC converter with common grounded input ports and continuous input current," *IEEE Transactions on Industrial Electronics*, vol. 69, no. 12, pp. 12859-12873, 2021.
[19] N. Bagheri, H. Alipour, L. Mohammadian, J. Beiza, and M. Ebadpour, "A Multiport isolated resonant LLC converter for grid-tied renewable energy powered bidirectional EV charger," *International Journal of Industrial Electronics Control and Optimization*, vol. 6, no. 1, pp. 37-48, 2023.
[20] G. Mohebalizadeh, H. Alipour, L. Mohammadian, and M. Sabahi, "A New Multi-Input DC/DC Converter with Coupled and Switched Inductor Applicable for Renewable Energy Sources," *International Journal of Industrial Electronics Control and Optimization*, vol. 5, no. 4, pp. 349-363, 2022.
[21] A. A. Asl, R. A. Asl, N. V. Kurdkandi, and S. H. Hosseini, "Modelling and controlling a new PV/FC/battery DC–DC converter suitable for DC motor," *The Journal of Engineering*, vol. 2022, no. 6, pp. 567-582, 2022.
[22] E. Babaei, Z. Saadatizadeh, and C. Cecati, "High step-up high step-down bidirectional DC/DC converter," *IET Power Electronics*, vol. 10, no. 12, pp. 1556-1571, 2017.
[23] K. Varesi, S. H. Hosseini, M. Sabahi, and E. Babaei, "Modular non-isolated multi-input high step-up dc-dc converter with reduced normalized voltage stress and component count," *IET Power electronics*, vol. 11, no. 6, pp. 1092-1100, 2018.
[24] S. Sathyan, H. M. Suryawanshi, A. B. Shitole, M. S. Ballal, and V. B. Borghate, "Soft-switched interleaved DC/DC converter as front-end of multi-inverter structure for microgrid applications," *IEEE Transactions on Power Electronics*, vol. 33, no. 9, pp. 7645-7655, 2017.
[25] A. Samadian, S. M. Hashemzadeh, M. G. Marangalu, M. Maalandish, and S. H. Hosseini, "A new dual-input high step-up DC-DC converter with reduced switches stress and low input current ripple," *IET Power Electronics*, vol. 14, no. 9, pp. 1669-1683, 2021.
[26] A. Mahmood et al., "A non-inverting high gain DC-DC converter with continuous input current," IEEE Access, vol. 9, pp. 54710-54721, 2021.
[27] R. Rajesh, N. Prabaharan, and T. Santhosh, "Design and analysis of a non-isolated DC-DC converter with a high-voltage conversion ratio," IEEE Transactions on Circuits and Systems II: Express Briefs, vol. 70, no. 6, pp. 2036-2041, 2022.



Hamed Abdi was born in Tabriz, Iran, completed his B.Sc. in Power Electrical Engineering at the University of Tabriz in 2019, and later pursued his M.Sc. in Power Electronics and Electrical Machines at the same institution, graduating in 2024. His academic journey has been marked by a commitment to excellence, as evidenced by his ranking as the top student in the Electrical Engineering department and his membership in the University's Talented Students Group.

Eng. Abdi has actively contributed to the field of electrical engineering through publications in reputable journals and conferences. His work includes power electronic converters, energy management systems for HEVs, and PV systems design. His dedication to advancing these areas has been recognized with accolades such as the Best Paper Award at the 16th Power Electronics & Drives: Systems and Technologies Conference (PEDESTC) in 2025.



Naghi Rostami was born in Ahar, Iran, in 1984. He received the B.Sc.degree from the Khajeh Nasir Toosi University of Technology, Tehran, Iran, in 2006, and the M.Sc. degree from the University of Tehran, Tehran, Iran, in 2008, and the ph.D. degree from the University of Tabriz, Tabriz, Iran, in 2013, all in electrical engineering.

He is currently an Assistant Professor at the Department of Electrical Engineering, University of Tabriz. He is involved with the electric machines branch with proficiency in finite-element software. His current research interests include electric machines and drives, and electric and hybrid vehicles.



Ebrahim Babaei received the Ph.D. degree in Electrical Engineering from the University of Tabriz, in 2007. He is the author and co-author of one book and more than 720 journal and conference papers. He also holds 26 patents in the area of power electronics. His current research interests include the analysis, modeling, design, and control of Power Electronics Converters and their applications, Renewable Energy Sources, and FACTS Devices.

Prof. Babaei has been the Editor-in-Chief of the Journal of Electrical Engineering of the University of Tabriz, since 2013. He was an Associate Editor of the IEEE Transactions on Industrial Electronics from 2015 to 2023. He is also currently an Associate Editor of the IEEE Transactions on Power Electronics, IEEE Open Journal of the Industrial Electronics Society, Iranian Journal of Science and Technology, Transactions of Electrical Engineering, and International Journal of Circuit Theory and Applications. He was selected by the Ministry of Science Research and Technology as the distinguished researcher of Iran in the field of engineering in 2022.



Bülent Bilgehan is the Dean of the Faculty of Engineering at Near East University. He holds a Ph.D. in Electrical and Electronics Engineering and specializes in Internet of Things (IoT), wireless communications, UAV systems, and intelligent optimization techniques. His research focuses on Industry 5.0, healthcare technologies, and disaster-resilient communication networks. Dr. Bilgehan has authored numerous publications in peer-reviewed journals and presented at international conferences. He actively leads national and international research projects and supervises graduate research in emerging technologies.